Optical phantoms of varying geometry based on thin building blocks with controlled optical properties

Daniel M. de Bruin
Rolf H. Bremmer
Vitali M. Kodach
University of Amsterdam
Academic Medical Center
Department of Biomedical Engineering and Physics
Amsterdam, 1100 DE Netherlands

Roy de Kinkelder
University of Amsterdam
Academic Medical Center
Department of Biomedical Engineering and Physics
Amsterdam, 1100 DE Netherlands
and
Topcon Europe Medical
b.v. Essebaan 11
Capelle aan den Ijssel, 2908 LJ Netherlands

Jan van Marle
University of Amsterdam
Academic Medical Center
Department of Cell Biology
Center for Microscopical Research
Amsterdam, 1100 DE Netherlands

Ton G. van Leeuwen
University of Amsterdam
Academic Medical Center
Department of Biomedical Engineering and Physics
Amsterdam, 1100 DE Netherlands
and
University of Twente
MIRA Institute for Biomedical Technology and Technical Medicine
Biomedical Photonic Imaging Group
Enschede, 7500 AE Netherlands

Dirk J. Faber
University of Amsterdam
Academic Medical Center
Department of Biomedical Engineering and Physics
and
Opthalmology Department
Amsterdam, 1100 DE Netherlands

Abstract. Current innovations in optical imaging, measurement techniques, and data analysis algorithms express the need for reliable testing and comparison methods. We present the design and characterization of silicone elastomer-based optical phantoms. Absorption is included by adding a green dye and scattering by adding TiO_2 or SiO_2 particles. Optical coherence tomography measurements demonstrate a linear dependence of the attenuation coefficient with scatterer concentration in the absence of absorbers. Optical transmission spectroscopy of the nonscattering absorbing phantoms shows a linear concentration dependent absorption coefficient. Both types of samples are stable over a period of 6 months. Confocal microscopy of the samples demonstrates a homogeneous distribution of the scatterers, albeit with some clustering. Based on layers with thicknesses as small as 50 μm, we make multifaceted structures resembling flow channels, (wavy) skin-like structures, and a layered and curved phantom resembling the human retina. Finally, we demonstrate the ability to incorporate gold nanoparticles within the phantoms. In conclusion, our phantoms are easy to make, are based on affordable materials, exhibit well-defined and controllable thickness, refractive index, absorption, and scattering coefficients, are homogeneous, and allow the incorporation of novel types of nanoparticle contrast agents. We believe our phantoms fulfill many of the requirements for an "ideal" tissue phantom, and will be particularly suited for novel optical coherence tomography applications.
[DOI: 10.1117/1.3369003]

Keywords: biomedical optics; imaging systems; optical properties; scattering; absorption.

Paper 09516R received Nov. 19, 2009; revised manuscript received Jan. 22, 2010; accepted for publication Jan. 26, 2010; published online Apr. 12, 2010.

1 Introduction

In today's clinical practice, optical monitoring and imaging techniques are indispensible in disease management. Morphological and functional information, ideally down to the cellular level, is needed for diagnosis, for monitoring response to therapy, and for follow-up after treatment. Optical imaging modalities range from the visualization of intracellular and intercellular processes through (confocal) microscopy to macroscopic imaging by optical tomography. In between, techniques such as optical coherence tomography (OCT) image down to 2 mm in depth at micrometer scale resolution. The interaction of light with tissue can also be used to acquire functional information of the tissue under study, such as oxygenation,[1] perfusion,[2] blood content, tissue viability, and chemical characterization of malformations.[3] Alongside instrumental developments, the integration of different techniques and the use of novel contrast agents such as gold

Address all correspondence to: University of Amsterdam, Academic Medical Center, Department of Biomedical Engineering and Physics, P.O. Box 22700, Amsterdam, 1100 DE Netherlands. Tel: 3120 5665179; E-mail: d.m.debruin@amc.nl

1083-3668/2010/15(2)/025001/10/$25.00 © 2010 SPIE

nanoparticles[4] are investigated to enable quantitative functional and molecular imaging of tissues.[5,6]

In vivo validation of these novel optical approaches is often difficult. Clinical acceptance requires proof of reproducible, device-independent, quantitative functional information in spite of the biological variability in the sought-after functional parameters. Moreover, for nanoparticle contrast agents, toxicity questions can exist. In such cases, the minimal detectable concentration of nanoparticle contrast agents needs to be determined *ex vivo* before their clinical use can be explored *in vivo*. For all these applications, tissue mimicking phantoms can play an essential role.[7–11]

Tissue often possesses structural inhomogeneity. Layers of different cell types can be formed, and cavities containing fluid and blood vessels can disrupt uniform tissue structures, all resulting in a structural complex geometry. Disease often manifests itself as a change in the morphology of the tissue (e.g., blood vessels in a tumor causing increased hemoglobin contrast or loss of layered architecture). It is therefore paramount that structural variations such as layers or inclusions can be incorporated in the phantom. An "ideal phantom" has a number of other properties,[12] of which controllable tissue-like scattering and absorption,[13] homogeneity,[14] tissue-like refractive index,[15] and durability[10] have been extensively investigated. Within individual layers or inclusions of a structured phantom, these desirable properties should still be applicable.

In this work, we describe the development of easy-to-manufacture, low-cost phantoms using 50 to 300-μm thin layers as building blocks, that fulfill the aforementioned desirable criteria. To our best knowledge, it is the first time that geometrical variations such as wavy structures mimicking the boundary between dermis and epidermis in skin and small capillary channels are demonstrated. The phantoms are characterized by OCT, transmission spectroscopy (TS), and confocal microscopy. To show that our approach enables construction of anatomically realistic phantoms that can be used in optical coherence tomography applications, images of a model eye/retina are presented. The latter is built from 50-μm thin layers with different scattering properties. This model can be used to compare segmentation methods of clinically used OCT systems and can test their reproducibility. In addition, we describe protocols to include gold nanoparticle contrast agents, and present layered phantoms to quantify the contrast caused by these particles in OCT images.

2 Materials and Methods

2.1 *Phantom Ingredients*

Silicone (Sylgard® 184 Silicone Elastomer DOW/Corning) is a two-component silicone product with a refractive index of 1.41, capable of curing at room temperature or at higher temperatures to shorten the curing time. Silicone therefore allows construction of complex geometries and easy incorporation of scatterers. The most important drawback of this material is its high hydrophobicity, which often makes mixing with a water-containing substance difficult.

To match the optical properties of tissue as close as possible, scattering and absorption spectra of the phantom need to be controlled. The scattering properties are determined by the refractive index mismatch between the matrix and the suspended particles. Various scattering particles have been proposed, including lipid microparticles (Intralipid), due to their cell mimicking bilipid membrane,[16,17] polymer microparticles (microspheres) owing to their exact controllable size,[18] and metal oxide powders like titanium dioxide (TiO_2).[19] Usually, absorption is controlled by mixing in suitable dyes.[20–23]

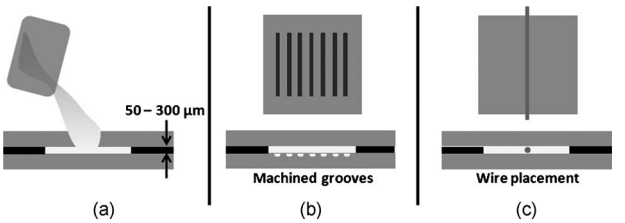

Fig. 1 Final steps in the phantom-making process. (a) Standard thin-layer phantoms are molded between two glass plates of 1-cm thickness. (b) One glass plate can be replaced with a machined plate with desired groove sizes. (c) Channels can be made by placing a wire within the phantom matrix material.

Scattering in our phantom building blocks is controlled by glass particles (SiO_2) with a refractive index of 1.37 at 589 nm and a radius of 500 ± 58 nm (Kisker Biotech, Germany). We were not able to construct homogeneous phantoms containing SiO_2 particles with weight percentages >1 w%. Given the small difference in refractive index between the particles and the matrix material, this composition did not cover the desired range of scattering coefficients found in tissues. We therefore also used titanium dioxide (TiO_2) with a refractive index of 2.49 (anatase form, Sigma Aldrich, Saint Louis, Missouri), and a mean radius of $\sim$50 nm with an unknown size distribution. Absorbing properties of the phantom are controlled by inclusion of ABS 551 (Exciton, Dayton, Ohio) dye. Moreover, we have been able to embed gold particles with a mean radius of $100 \text{ nm} \pm 2$ nm (Corpuscular, Cold Spring, New York). The various absorber or scatterer concentrations of all phantoms are based on weight percentage.

2.2 *Phantom Protocol*

Individual phantom layers are made by mixing the desired concentration of absorber and/or scatterer with the curing agent component of the silicone elastomer. To obtain a homogeneous mixture, the particles or dyes are forced to mix with the curing agent by using a tissue homogenizer with a very small spacing between tube and pillar (VWR Labshop, Batavia, Illinois). Next, the mixture is placed in an ultrasonic bath for 10 min at 30 kHz to break residual clusters. The curing agent is then mixed with the silicone (1 to 9 weight ratio) under careful stirring using a standard laboratory mixer for 30 min. Remaining air bubbles are removed by using a vacuum pump that keeps the mixture under low pressure condition for 5 min. As shown in Fig. 1(a), a small portion (0.5 ml) of the final mixture is placed between two thick glass plates, separated by two spacers of the desired phantom thickness (ranging from 50 to 300 μm). Finally, curing at 60 °C for 6 h or at room temperature for 24 h results in a thin single-layered phantom building block. Multiple layered phantoms are created by stacking the desired phantoms on top of each other. Accidental air bubbles between layers are re-

moved using a vacuum pump. Electrostatic forces keep the phantom layers together.

Geometrical complex phantoms like skin models with wavy structures are prepared by replacing one of the glass plates with a machined plate with the desired structured interface. This plate is then placed on top of the viscose matrix material before curing. After curing, both plates are removed, resulting in a structured phantom [Fig. 1(b)]. A second layer can also be molded on top of the first structured phantom and can be cured again, resulting in a multiple layered phantom model with incorporated structure. Flow channels can be made by placing thin (electrical) wires in the layer, which can be removed after curing by carefully pulling the wire out of the phantom [Fig. 1(c)].

Inclusion of gold particles in the phantom building blocks is challenging due to their high surface charge, which tends to lead to clustering when embedded in silicone elastomer. To avoid this, the gold particles are coated with polyethylene glycol (PEG 6000, Sigma Aldrich), a procedure used to couple antibodies to the gold particles when they are used as targeted contrast agents.[24] The PEG was added in equal amounts directly to 2-ml gold particle-water solution (4.1×10^9 particles/ml) at room temperature for at least 1 h. Subsequently, the particles were centrifuged at 6500 RPM for 20 min. The PEG-containing liquid was removed with a pipette. The pallet of gold nanoparticles was dispersed in the curing agent of the phantom material as described before for obtaining a homogeneous mixture with other particles. We constructed four layered phantoms consisting of TiO_2-based, nonabsorbing phantoms (μ_t=4 mm^{-1}, 50, 100, 150, and 200 μm thickness) placed on top of a 200-μm thin nanoparticle-containing phantom ($\sim 10^9$ particles/ml) using the procedures described before.

2.3 *Phantom Characterization*

To verify the scattering and absorption properties of the phantom building blocks, we quantified attenuation coefficients (μ_t) for various single-layered phantoms using OCT[5] and TS. Microscale homogeneity of the phantoms is assessed with confocal microscopy by measuring the particle size distribution inside the phantoms; macroscale homogeneity is assessed with OCT by fitting the attenuation coefficient in different regions of interest within the phantom. The refractive index of the phantoms is measured using OCT[25] in comparison with Gauge measurements. Durability is verified by comparison of OCT and TS measurements taken 24 h after curing, and after 6 months for scattering and 4 months for absorbing phantoms. Geometrical variations are visualized using OCT. These methods are discussed in more detail below.

2.4 *Optical Coherence Tomography*

The employed OCT system was a standard time domain system (TDOCT), operating at 850 nm, using a linearly moving mirror in the reference arm and dynamic focusing in the sample arm. The axial and lateral resolutions of the system were 14 and 5 μm, respectively, measured in air. The measured signal-to-noise ratio (SNR) was 118 dB. We verified that the power coupled back from the reference arm was constant over the scan range. Dynamic focusing is achieved by translating the sample arm lens in depth, during A-scan acquisition. This arrangement allows for precise measurements of the attenuation coefficient of weakly scattering media, as described in Refs. 5 and 26, because during the measurement, the positions of the coherence and confocal gates are matched. Using Beer's law, the detector current i_d of the system is described as

$$i_d \propto [\exp(-2\mu_t z)]^{1/2},$$

where μ_t is the attenuation coefficient and z is the depth of the light in the sample. The square root accounts for the fact that the detector current is proportional to the field returning from the sample, rather than intensity. The attenuation coefficient is then extracted from the OCT data by fitting Beer's law to the averaged A-scans from a selected region of interest in the OCT image ($\sim$100 A-scans of 4096 points, 1.5-mm scan length). Prior to fitting, all A-scans are aligned. The standard deviation corresponding to the average A-scan is used for weighting in the fitting procedure. The fit model features three parameters, an amplitude for scaling, the attenuation coefficient, and an offset, which is fixed at the mean noise level. An uncertainty estimate for the fitted μ_t is computed from the covariance matrix returned by the fitting algorithm, and is specified as 95% confidence intervals of the fitted μ_t. The curve fit typically included $\sim$1000 data points in the averaged A-scan. The refractive index of the phantoms is determined by the ratio of the optical path length measured with OCT and the geometrical path length measured with a precision Gauge tool.

Structural complex samples were visualized with a commercially available 50-kHz swept source OCT system [Santec (Aichi, Japan) HSL 2000, 10-μm axial resolution, 11-μm lateral resolution]. The retinal model was imaged with a Topcon (Tokyo, Japan) 3D-1000 O, Mark II system (6.75-μm axial resolution and 20-μm lateral resolution), operating at 830 nm, which is routinely used in the ophthalmology department of our hospital. No additional image enhancement was performed on the presented images.

Images of the gold-nanoparticle-containing phantoms are obtained using the TDOCT system described before (3.0 mm, 4096 points axially by 2.0 mm, and 1000 A-scans laterally). To enhance the visualization of the gold nanoparticles in the bottom layer of the phantom, the images are first median filtered (5×5 pixels); subsequently a contrast-to-noise ratio (CNR) filter is applied (the ratio of the signal standard deviation over mean in a 25×25 pixel window). Visibility of the nanoparticles in the image is further enhanced by applying a histogram equalization to redistribute the gray values. To quantitatively analyze the contrast caused by the nanoparticles, we calculated the CNR as a function of the optical density (OD) of the overlying phantom layer ($OD = \mu_t \times d$, where d is the phantom thickness). Mean CNR $\pm$ standard deviation was obtained from five 25×25 pixel windows in the unprocessed OCT image, from both the overlying layer and the gold-nanoparticle-containing layer.

2.5 *Optical Transmission Spectroscopy*

Optical transmission spectroscopy (TS) uses transmission of light to determine a material's optical properties, including scattering and absorption. This technique has demonstrated its value in various disciplines ranging from material science to

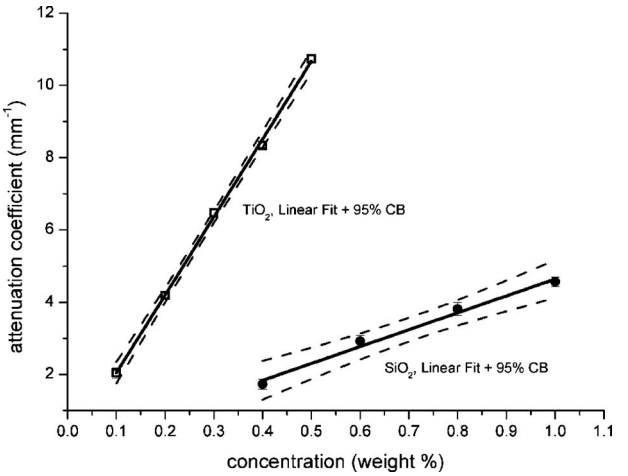

Fig. 2 Phantom attenuation coefficient (mm^{-1}) versus concentration (weight percent) of TiO_2 (□) and SiO_2 particles (●), measured with optical coherence tomography. Solid line is linear fit and dashed lines are 95% confidence bounds of the linear fit. For SiO_2 particles, the slope of the linear fit=4.67±0.31 mm^{-1}w%$^{-1}$ and offset μ_t=−0.34±0.22 mm^{-1} (R^2=0.986). For the TiO_2 particles, the slope =21.56±0.38 mm^{-1}weight^{-1} and offset μ_t=−0.11±0.11 mm^{-1} (R^2 =0.998).

tissue diagnostics, and is routinely used in medicine to determine the oxygen saturation of blood.[27] We utilized TS to investigate how the optical properties of our phantoms depend on the absorber concentration and whether they are stable in time. We illuminated the phantoms with a tungsten-halogen light source [Ocean Optics (Dunedin, Florida) DH-2000]. The light was collimated and coupled into a fiber probe with a 300-μm core diameter multimode fiber and directed at the phantom. The transmitted light was collected with a 300-μm multimode fiber and sent to a compact charge-coupled device (CCD) spectrometer (Ocean Optics, USB4000). Spectra were collected from 400 to 900 nm with 2-nm resolution. The attenuation coefficient was analyzed at the wavelengths corresponding to minimal (517 nm) and maximum (700 nm) absorption for all absorbing dye concentrations.

2.6 *Confocal Microscopy*

Microscale homogeneity of the phantom building blocks is assessed by estimating the size distribution of the embedded particles from a set of confocal microscopy images. Images were obtained using a Leica TCS SPII2 AOBS system, in which samples were imaged with 561-nm light in reflective mode. A 40/NA 1.25 oil immersion objective was used, resulting in a transversal resolution of approximately Δx, Δy=340 nm full width at half maximum (FWHM) and an axial resolution of Δz=1400 nm. The confocal voxel size was (x=240 nm, y=240 nm, and z=410 nm) for the images of SiO_2-based phantoms, and (x=80 nm, y=80 nm, and z=490 nm) for images of TiO_2-based phantoms. Note that the resolution exceeds the radii of the SiO_2 and TiO_2 particles, so that the estimated size distribution is a convolution of the actual size distribution with the response function of the confocal microscope. Particles are detected in each image by first applying a 5×5 pixel Laplacian filter to enhance the contours of the particles, followed by an intensity threshold to remove noise (at gray level 146 of 255). Subsequently, the image is converted to binary (pixel values 0 or 1), where all pixels within a particle's contour are set to 1. Particles at the boundary of the image, and particles not resistant to a 3×3 pixel erosion operation, are removed from the image. The remaining particles are assigned a unique number, which is stored along with center coordinates, area, and mean intensity calculated from the original image. Large particles or clusters of particles may appear in more than one image in the stack. To account for this, particle numbers are reassigned for particles that have their center coordinates within the bounding rectangle of any particle appearing in the subsequent image. When a particle appears in more than one image, the record with the highest mean intensity is kept. After this pro-

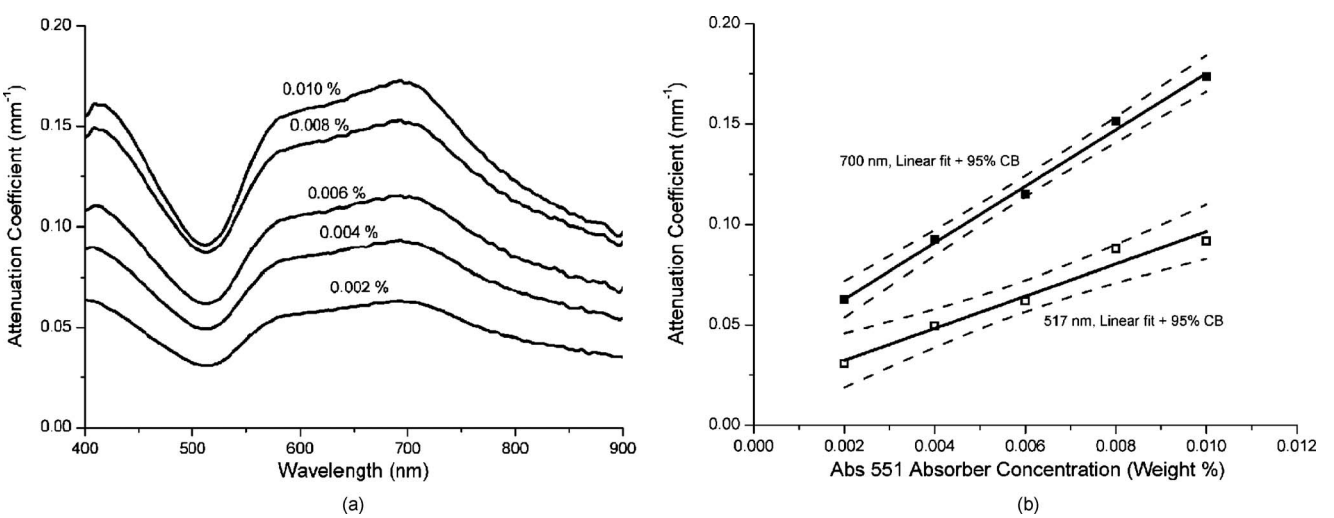

Fig. 3 Attenuation spectra of five different nonscattering phantoms with ABS 551 absorber versus concentration. (a) Uncertainties of the data points are smaller than symbol size. (b) Attenuation coefficient (mm^{-1}) versus absorber concentration (weight %) at 517 nm (□) and at 700 nm (●). Solid lines show linear fits; dashed lines indicate the 95% confidence bounds of the linear fits. At 517 nm, the slope was 8.01±0.87 mm^{-1}w%$^{-1}$; offset: μ_t=0.016±0.006 mm^{-1}; and R^2=0.95. At 700 nm, the slope was 14.07±0.58 mm^{-1}w%$^{-1}$; offset: μ_t=0.035±0.004 mm^{-1}; and R^2=0.99.

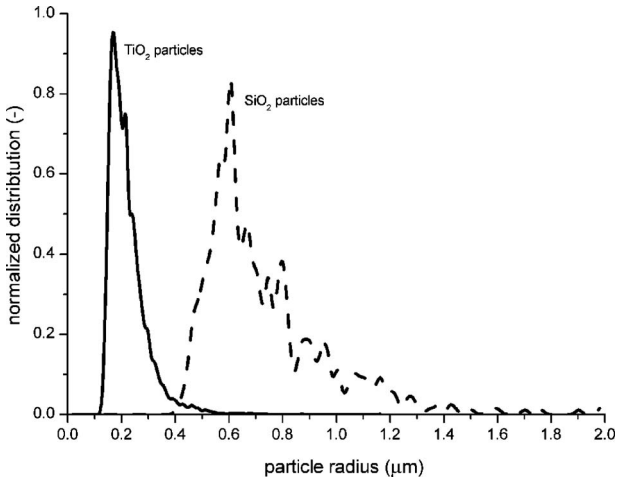

Fig. 4 Estimated size distribution of particle radius inside 300-μm phantoms obtained from confocal microscopy. Dashed line: phantom containing 1 weight procent SiO_2 particles. Mean: 220 nm; SD: 630 nm; skewness: 0.43; solid line: phantom containing 0.5 weight procent TiO_2 particles. Mean: 730 nm; SD: 600 nm; skewness: 0.6.

cess, for each remaining particle an equivalent radius is calculated from $r=\sqrt{(\text{area}/\pi)}$, which finally yields the estimate of the size distribution. The asymmetry of this obtained distribution is assumed to be proportional to the asymmetry of the actual size distribution.

3 Results

OCT imaging of nonabsorbing phantoms of 300-μm thickness with varying concentrations of SiO_2 and TiO_2 scattering particles was performed. From the OCT data, fitting the attenuation coefficients using Beer's law (Fig. 2) showed linear relations between attenuation coefficient and concentration, $\mu_t=4.67\pm0.31$ mm^{-1}/(weight percent) with an $R^2=0.986$ for the SiO_2 phantoms, and $\mu_t=21.56\pm0.38$ mm^{-1}/(weight percent) with an $R^2=0.998$ for TiO_2 phantoms. The intercepts of both curves, $\mu_t=-0.34\pm0.22$ mm^{-1} and $\mu_t=-0.11\pm0.11$ mm^{-1}, show that there is no significant absorption or scattering by the matrix material in these phantoms at 850 nm. Figure 3(a) shows transmission spectra of 1-cm-thick nonscattering phantoms containing the green dye as an absorber with five different concentrations (0.002 to 0.01 weight percent), measured with TS. In Fig. 3(b) attenuation spectra are shown for 517 nm [$\mu_t=8.01\pm0.87$ mm^{-1}/(weight percent); $R^2=0.95$]; and 700 nm [$\mu_t=14.07\pm0.58$ mm^{-1}/(weight percent); $R^2=0.99$], corresponding to minimal and maximal absorption. Again, a linear relation between attenuation coefficient and concentration was found. The intercepts of 0.016 ± 0.006 mm^{-1} for the 517-nm measurement and 0.035 ± 0.004 mm^{-1} for the 700-nm measurement indicate there is some residual scattering or absorption by the matrix material at these wavelengths.

Figure 4 shows size distributions measured inside 300-μm thin phantoms obtained from confocal microscopy. The dashed line shows the size distribution obtained from a phantom containing 1 weight percent SiO_2 particles. According to the manufacturer, the size distribution of the SiO_2 particles is normal, with a mean radius of 500 nm and standard deviation of 58 nm. Calculations on the measured distribution reveal a mean radius of 730 nm with a standard deviation of 600 nm. Note that we did not correct these results for transversal resolution of the confocal microscope (FWHM 340 nm). The positive skewness (0.6 versus 0 for a normal distribution) reveals the asymmetry of the distribution toward larger particle radii. This suggests that some clustering has taken place in the phantoms. The solid line shows the distribution obtained from a phantom containing 0.5 weight percent TiO_2 particles. As for the SiO_2 particles, the data are not deconvolved to account for the transversal resolution of the microscope; the determined distribution therefore deviates from the expected $r=100$ nm. We found a mean of 220 nm, standard deviation of 630 nm, and positive skewness of 0.43. This indicates clustering at the microscopic level.

Macroscale homogeneity was verified with OCT for the five different concentrations of TiO_2 scattering phantoms. Attenuation coefficients were measured in three different regions of interest within each phantom (μ_t roi1, μ_t roi2, and μ_t roi3). From these measurements, the average attenuation coefficient (mean μ_t) and SD were calculated (Table 1). The variation in μ_t (SD/mean expressed as a percentage) was less than 8.5% for these phantoms. Similar results were obtained for the SiO_2

Table 1 Macrohomogeneity measured with OCT. Each concentration is measured using three different regions of interests within the phantom.

OCT at 850 nm					
Concentration weight %	μ_t roi1 mm^{-1}	μ_t roi2 mm^{-1}	μ_t roi3 mm^{-1}	Mean μ_t±SD mm^{-1}	$\Delta\ \mu_t$ %
0.1	1.75	2.00	1.93	1.89±0.16	8.5
0.2	4.25	5.15	5.17	4.86±0.08	1.6
0.3	7.50	7.64	6.73	7.29±0.21	2.9
0.4	8.21	8.29	8.75	8.42±0.29	3.4
0.5	10.00	11.30	11.6	10.97±0.38	3.4

Table 2 Thickness measurements of 300-μm-thick phantoms measured with OCT and a precision Gauge tool, and corresponding calculated refractive indices.

Phantom number	Optical thickness (μm)	Geometrical thickness (μm)	Refractive index n
1	473	332	1.43
2	465	325	1.43
3	441	311	11.42
4	509	360	1.41
5	438	312	1.41
Mean ± sd	465 ± 29	328 ± 20	1.42 ± 0.01

phantoms with a variation in μ_t less than 7.3%.

Tissue-comparable refractive indices were determined for five different phantoms using OCT (Table 2). Optical path length measurements with OCT showed a mean thickness of 465 ± 29 μm, and Gauge measurements showed a mean thickness of 328 ± 20 μm. This resulted in a mean refractive index of 1.42 with standard deviation of 0.01, which is close to the value specified by the manufacturer (1.41).

Durability was verified using OCT and TS. As shown in Table 3, measured μ_t 24 h after curing (t1) and after 6 months (t2) showed small changes of less than 15% increase in scattering TiO_2 phantoms. These variations are larger than the variations in macroscale homogeneity reported in Table 1. Nonscattering phantoms containing only absorber measured with TS 24 h after curing (t1) and after 4 months (t2) also showed small changes (less than 5%), except for the 0.008% weight concentration phantom (Table 4).

Structural variations were visualized with OCT. Figure 5(a) demonstrates a skin model with wavy structures within two layers representing dermis and epidermis. Figure 5(b) represents the 3-D reconstruction of the skin phantom. Figure 5(c) depicts a vascular phantom model with a vessel of 200 μm. This phantom is constructed from a 0.4 and 0.1% TiO_2 phantom layer with a 20% Intralipid-filled channel within the bottom layer. Figure 5(d) represents the 3-D reconstruction of the vascular phantom.

Table 3 Durability measurements of TiO_2 phantoms; t1 is 24 h after curing, and t2 is after 6 months.

OCT at 850 nm				
Concentration weight %	μ_t t1 mm^{-1}	μ_t t2 mm^{-1}	$\Delta\ \mu_t$ mm^{-1}	$\Delta\ \mu_t$ %
0.1	2.04	2.34	0.30	15
0.2	4.19	4.77	0.58	14
0.3	6.47	7.18	0.71	11
0.4	8.34	9.53	1.19	14
0.5	10.74	11.21	0.47	4

Table 4 Durability measurements of ASB 551 phantoms; t1 is 24 h after curing, and t2 is after 4 months.

TS at 700 nm				
Concentration weight %	μ_t t1 mm^{-1}	μ_t t2 mm^{-1}	$\Delta\ \mu_t$ mm^{-1}	$\Delta\ \mu_t$ %
0.002	0.063	0.060	−0.003	−4.8
0.004	0.093	0.095	0.002	2.2
0.006	0.115	0.114	−0.001	−0.9
0.008	0.152	0.212	0.060	39
0.010	0.174	0.169	−0.005	−2.9

OCT images of the model eye/retina taken with the Topcon 3-D OCT system are depicted in Fig. 6(a). This phantom model is constructed from alternating 0.5% (μ_t=11 mm^{-1}) and 0.2% (μ_t=4 mm^{-1}) TiO_2 phantom layers, fixed in a curved holder placed in a water-filled chamber. The 50-μm-thick layers are clearly distinguishable from each other. Also visible is the adhesive tape used to fix the phantom in the eye, which shows up as a relatively transparent layer. Figure 6(b) is a schematic overview of the different parts of the model eye. Figure 6(b) part *a* shows the water-filled cube. A lens is positioned at the position shown by part *b*, the retina holder shown by part *c* can be placed inside the cube on a translation stage, shown by part *d*. The translation stage allows for changing the position of the retina holder. The cube

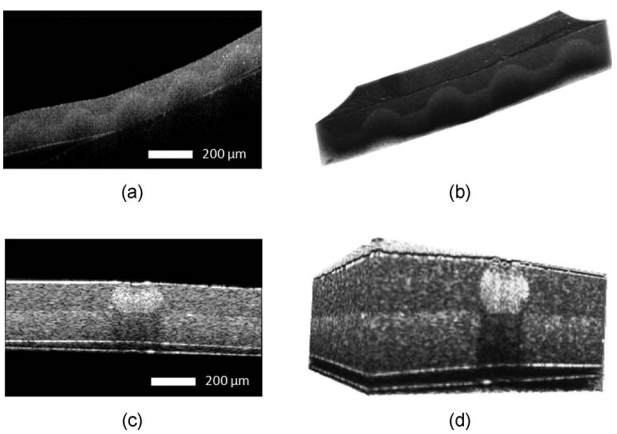

Fig. 5 Geometrical variations of TiO_2 particles containing phantoms obtained with the Santec OCT system. (a) Skin simulating phantom resembling the wavy dermal and epidermal structure of skin. (b) 3-D reconstruction of the skin phantom reconstructed from 250 B-scans. (c) Small 200-μm channel within a 300-μm-thick phantom layer. The phantom is constructed from a 300-μm thin top layer (0.1% TiO_2) and a 300-μm thin bottom layer (0.4% TiO_2), which includes the vessel filled with 20% Intralipid. (d) 3-D reconstruction of the channel phantom reconstructed from 250 B-scans.

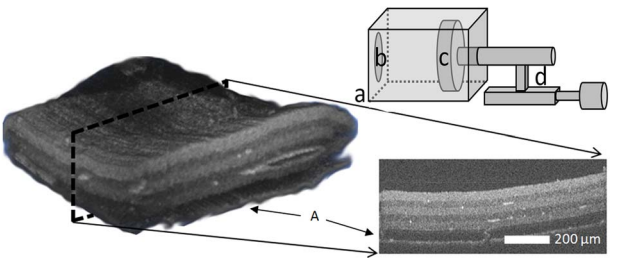

Fig. 6 (a) Retinal phantom model imaged with the Topcon 3D, depicting the cross sectional image of the retina phantom and reconstructed 3-D image. Individual layers are 50 μm thin. A indicates adhesive tape. (b) Inset: Model eye with **a** water filled chamber; **b** is f=20 mm achromat; **c** represents retina phantom; and **d** is eye length control.

can be closed with a water-sealed transparent lid on top.

Figure 7(a), top row, shows a fused image from four OCT datasets taken with our time-domain OCT system at 850 nm. A phantom of 200-μm thickness, containing approximately 10^9 gold nanoparticles per ml, is placed underneath a stack of 50-μm thin TiO_2 containing phantoms with μ_t=4 mm^{-1}. The nanoparticles show up as bright spots in the OCT images, although they become less visible with increasing layer thickness (or OD) of the top layer. Labels in the figure indicate the thickness of the overlying layer. The lower row of Fig. 7(a) is a processed version of the upper image, in which the visibility of the nanoparticles is enhanced by subsequent median filtering and contrast-to-noise ratio calculation. In Fig. 6(b) we quantified the decrease of visibility with OD by calculating the contrast-to-noise ratio in five 25×25 pixel windows in the phantom layer containing the gold nanoparticles (open squares). For reference, CNR was also calculated in the overlying phantom layer (solid circles). With increasing OD of the overlying layer, the CNR in the nanoparticle-containing layer decreases to ~40% of its starting value, confirming the qualitative observations from the OCT images. Figure 7(b) shows that for the present combination of nanoparticles, sample, and OCT system, the nanoparitcles cause detectable contrast with the optical density of the overlying layer up to OD=0.4. For higher OD, the particles are present but their signal is not strong enough to be differentiated from the background. The CNR in the overlying layer is independent of the layer thickness, as expected for a homogeneous sample.

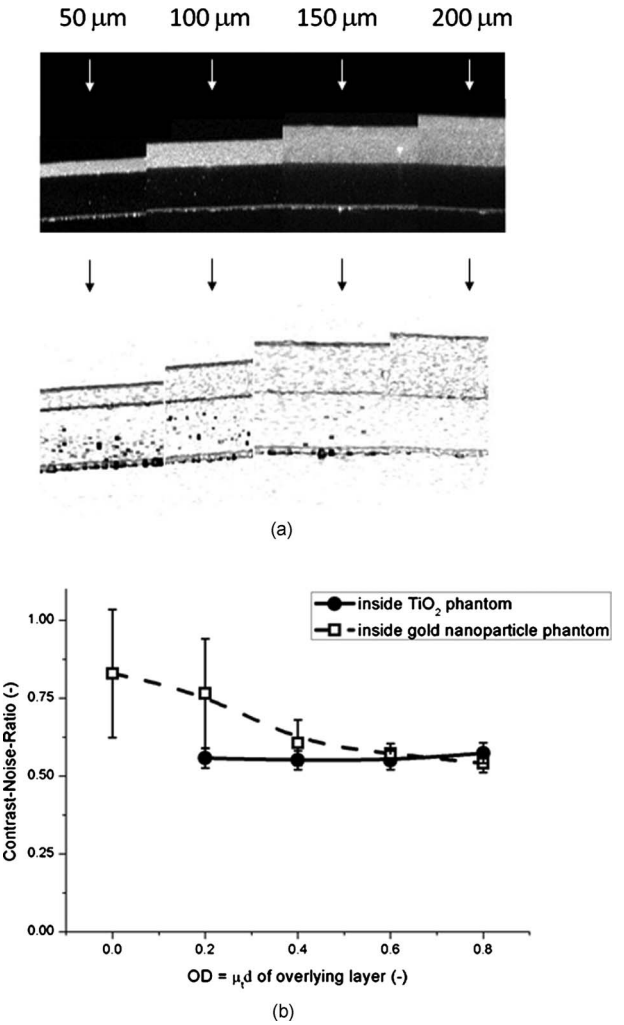

Fig. 7 (a) Compounded OCT images of four double-layered phantoms, with gold nanoparticles in the bottom layer (200 μm, ~10^9 gold nanoparticles/ml). Top layers are 50, 100, 150, and 200-μm thin phantoms containing TiO_2 particles (μ_t=4 mm^{-1}). Lower image is a filtered version of the top image to enhance the visibility of the nanoparticles. (b) Visibility (contrast-to-noise ratio) versus OD=$\mu_t d$ of the overlying layer in the phantom layer containing the gold nanoparticles (□) and in the overlying phantom layer (●).

4 Discussion

We demonstrated that homogeneous and durable silicone elastomer-based optical phantoms can be constructed using thin layers of 50 μm as building blocks, with controllable thickness, absorption, and scattering properties, refractive index, and they allow multifaceted structural variations resembling flow channels and wavy skin-like structures. We constructed a curved multilayered human retina phantom as an example. Novel types of contrast agents can also be incorporated. The phantoms are based on affordable materials, are easy to make, and fulfill many of the criteria for an "ideal phantom" as stated by Pogue et al.[12] We believe that this advanced class of phantoms is important for characterizing new and already existing optical techniques used in the clinic. Layers thinner than 50 μm can in principle be fabricated, although the curing process may then take longer than 6 h.

Our confocal microscopy results indicate that some microscopic clustering of the particles takes place. However, from the macroscale homogeneity study by OCT, we conclude that our phantom protocol is repeatable, and that Figs. 2 and 3 can be used to predict the optical properties as functions of phantom ingredients. Still, individual characterisation of phantoms is recommended.

The feasibility to incorporate molecules of specific interest (e.g., fluorophores) in a phantom building block is largely determined by the chosen matrix material and is closely related to our process of including nanoparticle contrast agents. The silicon matrix used in our phantoms is hydrophobic, which means that inclusion of biological chromophores may be challenging. For example, the absorption spectrum of the ABS 551 dye used in the measurements presented in Fig. 3

changed from its original spectrum supplied by the manufacturer during the curing process, which is probably due to a reaction with the curing agent. The original spectra were measured in methylene chloride, which is significantly different from a silicone elastomer. Nevertheless, after curing, the absorption spectra were stable. This behavior also suggests that mixing in fluorophores will not always be trivial. On the other hand, several absorbers specifically designed for silicone are available.[28] The minimal changes in optical properties over time can be contributed to the fact that all components are inorganic and chemically stable. Initial experiments in our laboratory show that it is even feasible to include red blood cells in the phantoms without significantly altering their spectral signature. Therefore, inclusion of specific molecules may be possible using appropriate encapsulation strategies while still maintaining their spectral properties. This might be achieved using a comparable PEGilation process as described with the gold nanoparticles. Although confocal microscopy (Fig. 4) and OCT images showed homogeneity (Table 4), it was suggested by Bisaillon et al.[10] that better homogeneity might be obtained by mixing hexane with silicone resin, which results in a low-viscose but still-curable silicone mixture.

The phantom material has various avantages. The two-component silicon matrix allows variation of the mechanical properties by changing the component ratios. Silicon phantoms therefore have been used for elastography applications.[29] The ability to incorporate Brownian motion or flow in the phantom is possible by including flow channels or compartments containing fluids inside the sample. In this work we have already demonstrated a flow channel. Including a compartment containing fluid in Brownian motion that mimics perfusion will be more challenging, but we believe feasible. Assuming that the thermal properties of the phantom are determined by the thermal conductivity of the matrix material (0.17 W/mK), this parameter is also in the same order of magnitude of most values found for soft tissues (0.1 to 0.7 W/mK).[30]

The time to manufacture a phantom according to the protocol presented in this work is approximately 8 h (including curing). Material costs of a phantom containing TiO_2 particles and absorber is estimated at approximately €2 per phantom; phantoms with more expensive SiO_2 particles are estimated to be approximately €50 per phantom for the highest concentration. The solid phantoms do not interact with their environment and are consequently easily transportable. Covered transportation is desirable to keep the phantoms clean, since dust is attracted due to high surface tension of the silicone.

4.1 *Potential Applications*

We demonstrated the application of our phantoms in optical coherence tomography, However, structured phantoms can be of enormous benefit for other optical modalities as well. A thin-layered phantom configuration might be able to evaluate diagnostic modalities that use spectral fitting procedures such as differential path-length spectroscopy and TS.[31–33] By combining absorbers and scatterers in one phantom layer, or by stacking scattering and absorbing layers on top of each other, the influence of absorption and scattering can be evaluated. The thin layers with well-defined optical properties can also serve as calibration samples for integrating sphere measurements.[34] Due to the elastic properties of the matrix material, the phantoms might also be used in photoacoustic systems. The acoustic wave propagation depends on the density and elasticity of the medium.[35] These values can be varied by changing the ratio between the silicone elastomer and curing agent, the two components of the matrix material.

The most common clinical application of OCT is in ophthalmology, where it is used to image the anterior and posterior parts of the eye.[36,37] Many clinical decisions rely on segmentation of OCT images and subsequent analysis of these segmented layers (e.g., thickness measurements). However, mechanical wear (for example, of galvoscanners), electro-optical wear (compromising performance of the light source), and digital issues (analysis software updates) may cause the outcome of such analyses to change over time, with the associated clinical consequences. Accurate and frequent calibration of these systems and methods is needed.[38,39] Thin-layered phantoms such as presented here are well suited for this purpose. To demonstrate this, we constructed a model eye using our phantoms to represent the retina (Fig. 6).

Recently, the use of nanoparticle contrast agents for (molecular contrast) OCT has received much attention. Before clinical acceptance of this technique, questions regarding the toxicity and clearing of these nanoparticles need to be resolved. In our opinion, the minimal concentration of nanoparticles that causes a signal that is distinguishable from the OCT background signal [minimal detectable dose (MDD)] needs to be determined first. The MDD will then serve as a starting point for toxicity studies.[4,40] The MDD will depend on the optical properties of the nanoparticles, the optical properties of the tissue they are applied to, and the technical characteristics of the OCT system used to detect them. Using our phantoms, it is possible to correlate the OCT signal to a controlled amount of nanoparticles at a controlled location in the sample with controlled optical properties. Figure 7(b) shows that for the present combination of nanoparticles, sample, and OCT system, the nanoparticles cause detectable contrast with the optical density of the overlying layer, up to OD=0.4. For higher OD, the particles are present but their signal is not strong enough to be differentiated from the background.

5 Conclusions

The validation of novel biomedical optical imaging techniques requires phantoms that allow creation of complex geometrical structures and inclusion of novel types of contrast agents. We show the design and characterization of silicone elastomer-based optical phantoms. For the first time, thin complex structures approaching real tissue geometry are demonstrated. Moreover, these phantoms exhibit well-defined controllable absorption and scattering properties. We present phantoms with attenuation coefficients ranging from 2 to 11 mm^{-1}, scaling linearly with scatterer concentration. The phantoms are characterized using optical coherence tomography, confocal microscopy, and transmission spectroscopy. The phantoms demonstrate good microscopic and macroscopic homogeneity, and have a tissue-comparable refractive index of 1.42 ± 0.01. The phantoms, tested by repeated OCT and TS attenuation measurements after 6 months, show small changes in the optical properties over

time. We believe our phantoms fulfill many of the requirements for an "ideal" tissue phantom, and will be particularly suited for novel optical coherence tomography applications.

Acknowledgments

This research is funded by a personal grant to Faber in the Vernieuwingsimpuls program (AGT07544) by the Netherlands Organization of Scientific Research (NWO) and the Technology Foundation STW. Kodach and de Kinkelder are supported by the IOP Photonic Devices program managed by the Technology Foundation STW and SenterNovem. We would like to thank M.J.C. van Gemert for constructive review of the manuscript. In addition, we would like to thank A. Steenbeek and C. Kools from the Department of Medical Instrumentation and Development, Academic Medical Center, for their contribution to this work.

References

1. D. J. Faber, E. G. Mik, M. C. G. Aalders, and T. G. van Leeuwen, "Light absorption of (oxy-)hemoglobin assessed by spectroscopic optical coherence tomography," *Opt. Lett.* **28**(16), 1436–1438 (2003).
2. M. C. G. Aalders, M. Triesscheijn, M. Ruevekamp, M. de Bruin, P. Baas, D. J. Faber, and F. A. Stewart, "Doppler optical coherence tomography to monitor the effect of photodynamic therapy on tissue morphology and perfusion," *J. Biomed. Opt.* **11**(4), 044011 (2006).
3. C. A. Patil, N. Bosschaart, M. D. Keller, T. G. van Leeuwen, and A. Mahadevan-Jansen, "Combined Raman spectroscopy and optical coherence tomography device for tissue characterization," *Opt. Lett.* **33**(10), 1135–1137 (2008).
4. J. L. West and N. J. Halas, "Engineered nanomaterials for biophotonics applications: improving sensing, imaging, and therapeutics," *Annu. Rev. Biomed. Eng.* **5**, 285–292 (2003).
5. D. J. Faber, F. J. van der Meer, and M. C. G. Aalders, "Quantitative measurement of attenuation coefficients of weakly scattering media using optical coherence tomography," *Opt. Express* **12**(19), 4353–4365 (2004).
6. S. C. Kanick, H. Sterenborg, and A. Amelink, "Empirical model description of photon path length for differential path length spectroscopy: combined effect of scattering and absorption," *J. Biomed. Opt.* **13**(6), 064042 (2008).
7. G. Wagnieres, S. G. Cheng, M. Zellweger, N. Utke, D. Braichotte, J. P. Ballini, and H. vandenBergh, "An optical phantom with tissue-like properties in the visible for use in PDT and fluorescence spectroscopy," *Phys. Med. Biol.* **42**(7), 1415–1426 (1997).
8. M. Firbank and D. T. Delpy, "A design for a stable and reproducible phantom for use in near-infrared imaging and spectroscopy," *Phys. Med. Biol.* **38**(6), 847–853 (1993).
9. T. S. Troutman, J. K. Barton, and M. Romanowski, "Optical coherence tomography with plasmon resonant nanorods of gold," *Opt. Lett.* **32**(11), 1438–1440 (2007).
10. C. E. Bisaillon, G. Lamouche, R. Maciejko, M. Dufour, and J. P. Monchalin, "Deformable and durable phantoms with controlled density of scatterers," *Phys. Med. Biol.* **53**(13), N237–N247 (2008).
11. C. E. Bisaillon, M. M. Lanthier, M. L. Dufour, and G. Lamouche, "Durable coronary artery phantoms for optical coherence tomography," *Proc. SPIE* **7161**, 71612E (2009).
12. B. W. Pogue and M. S. Patterson, "Review of tissue simulating phantoms for optical spectroscopy, imaging and dosimetry," *J. Biomed. Opt.* **11**(4), 041102 (2006).
13. T. Moffitt, Y. C. Chen, and S. A. Prahl, "Preparation and characterization of polyurethane optical phantoms," *J. Biomed. Opt.* **11**(4), 041103 (2006).
14. A. J. Durkin, S. Jaikumar, and R. Richardskortum, "Optically dilute, absorbing, and turbid phantoms for fluorescence spectroscopy of homogeneous and inhomogeneous samples," *Appl. Spectrosc.* **47**(12), 2114–2121 (1993).
15. X. Y. Wang, C. P. Zhang, L. S. Zhang, L. L. Xue, and J. G. Tian, "Simultaneous refractive index and thickness measurements of bio tissue by optical coherence tomography," *J. Biomed. Opt.* **7**(4), 628–632 (2002).
16. H. J. van Staveren, C. J. M. Moes, J. van Marle, S. A. Prahl, and M. J. C. van Gemert, "Light-scattering in intralipid-10-percent in the wavelength range of 400–1100 nm," *Appl. Opt.* **30**(31), 4507–4514 (1991).
17. S. T. Flock, S. L. Jacques, B. C. Wilson, W. M. Star, and M. J. C. Van Gemert, "Optical-properties of intralipid—a phantom medium for light-propagation studies," *Lasers Surg. Med.* **12**(5), 510–519 (1992).
18. J. M. Schmitt, A. Knuttel, and R. F. Bonner, "Measurement of optical-properties of biological tissues by low-coherence reflectometry," *Appl. Opt.* **32**(30), 6032–6042 (1993).
19. M. I. Cabrera, O. M. Alfano, and A. E. Cassano, "Absorption and scattering coefficients of titanium dioxide particulate suspensions in water," *J. Phys. Chem.* **100**(51), 20043–20050 (1996).
20. E. L. Hull, M. G. Nichols, and T. H. Foster, "Quantitative broadband near-infrared spectroscopy of tissue-simulating phantoms containing erythrocytes," *Phys. Med. Biol.* **43**(11), 3381–3404 (1998).
21. S. J. Madsen, M. S. Patterson, and B. C. Wilson, "The use of india ink as an optical absorber in tissue-simulating phantoms," *Phys. Med. Biol.* **37**(4), 985–993 (1992).
22. U. Sukowski, F. Schubert, D. Grosenick, and H. Rinneberg, "Preparation of solid phantoms with defined scattering and absorption properties for optical tomography," *Phys. Med. Biol.* **41**(9), 1823–1844 (1996).
23. M. S. Patterson and B. W. Pogue, "Mathematical-model for time-resolved and frequency-domain fluorescence spectroscopy in biological tissue," *Appl. Opt.* **33**(10), 1963–1974 (1994).
24. C. Loo, L. Hirsch, M. H. Lee, E. Chang, J. West, N. Halas, and R. Drezek, "Gold nanoshell bioconjugates for molecular imaging in living cells," *Opt. Lett.* **30**(9), 1012–1014 (2005).
25. A. Knuttel, S. Bonev, and W. Knaak, "New method for evaluation of *in vivo* scattering and refractive index properties obtained with optical coherence tomography," *J. Biomed. Opt.* **9**(2), 265–273 (2004).
26. T. G. van Leeuwen, D. J. Faber, and M. C. Aalders, "Measurement of the axial point spread function in scattering media using single-mode fiber-based optical coherence tomography," *IEEE J. Sel. Top. Quantum Electron.* **9**(2), 227–233 (2003).
27. A. A. Stratonnikov and V. B. Loschenov, "Evaluation of blood oxygen saturation *in vivo* from diffuse reflectance spectra," *J. Biomed. Opt.* **6**(4), 457–467 (2001).
28. S. P. Haug, C. J. Andres, and B. K. Moore, "Color stability and colorant effect on maxillofacial elastomers. Part I: colorant effect on physical properties," *J. Prosthet. Dent.* **81**(4), 418–422 (1999).
29. J. B. Fowlkes, S. Y. Emelianov, J. G. Pipe, A. R. Skovoroda, P. L. Carson, R. S. Adler, and A. P. Sarvazyan, "Magnetic-resonance imaging techniques for detection of elasticity variation," *Med. Phys.* **22**(11), 1771–1778 (1995).
30. C. S. Orr and R. C. Eberhart, "Overview of bioheat transfer," in *Optical-Thermal Response of Laser-Irradiated Tissue*, A. J. Welch and M. J. C. Gemert, Eds., pp. 367–384, Plenum, New York (1995).
31. A. Amelink and H. Sterenborg, "Measurement of the local optical properties of turbid media by differential path-length spectroscopy," *Appl. Opt.* **43**(15), 3048–3054 (2004).
32. A. Amelink, H. Sterenborg, M. P. L. Bard, and S. A. Burgers, "*In vivo* measurement of the local optical properties of tissue by use of differential path-length spectroscopy," *Opt. Lett.* **29**(10), 1087–1089 (2004).
33. S. L. Jacques and B. W. Pogue, "Tutorial on diffuse light transport," *J. Biomed. Opt.* **13**(4), 041302 (2008).
34. J. W. Pickering, S. A. Prahl, N. van Wieringen, J. F. Beek, H. Sterenborg, and M. J. C. van Gemert, "Double-integrating-sphere system for measuring the optical-properties of tissue," *Appl. Opt.* **32**(4), 399–410 (1993).
35. C. G. A. Hoelen, F. F. M. de Mul, R. Pongers, and A. Dekker, "Three-dimensional photoacoustic imaging of blood vessels in tissue," *Opt. Lett.* **23**(8), 648–650 (1998).
36. D. Huang, E. A. Swanson, C. P. Lin, J. S. Schuman, W. G. Stinson, W. Chang, M. R. Hee, T. Flotte, K. Gregory, C. A. Puliafito, and J. G. Fujimoto, "Optical coherence tomography," *Science* **254**(5035), 1178–1181 (1991).
37. B. Cense, N. A. Nassif, T. Chen, M. Pierce, S. H. Yun, B. H. Park, B. E. Bouma, G. J. Tearney, and J. F. de Boer, "Ultrahigh-resolution high-speed retinal imaging using spectral-domain optical coherence tomography," *Opt. Express* **12**(11), 2435–2447 (2004).
38. H. W. van Dijk, P. H. B. Kok, M. Garvin, M. Sonka, J. H. de Vries, R. P. Michels, M. E. J. van Velthoven, R. O. Schlingemann, F. D. Verbraak, and M. D. Abramoff, "Selective loss of inner retinal layer

thickness in type 1 diabetic patients with minimal diabetic retinopathy," *Invest. Ophthalmol. Visual Sci.* **50**, 3404–3409 (2009).
39. D. M. de Bruin, D. Burnes, J. Loewenstein, Y. Chen, S. Chang, T. Chen, D. Esmaili, and J. F. de Boer, "*In vivo* three-dimensional imaging of neovascular age related macular degeneration using optical frequency domain imaging at 1050 nm," *Invest. Ophthalmol. Visual Sci.* **49**, 4545–4552 (2008).
40. M. E. J. van Velthoven, D. J. Faber, F. D. Verbraak, T. G. van Leeuwen, and M. D. de Smet, "Recent developments in optical coherence tomography for imaging the retina," *Prog. Retin Eye Res.* **26**(1), 57–77 (2007).